Received: 16 September 2024 | Revised: 5 November 2024 | Accepted: 5 December 2024

DOI: 10.1002/dro2.163

Droplet Open Access WILEY

RESEARCH ARTICLE

Reconsideration on the maximum deformation of droplets impacting on solid surfaces

Zhifeng Hu[1,2] | **Haojiang Ran**[3,4] | **He Shan**[1] | **Fuqiang Chu**[2,3] | **Zuankai Wang**[2] |
Ruzhu Wang[1]

[1] Institute of Refrigeration and Cryogenics, MOE Engineering Research Center of Solar Power & Refrigeration, Shanghai Jiao Tong University, Shanghai, China

[2] Department of Mechanical Engineering, The Hong Kong Polytechnic University, Hong Kong, China

[3] School of Energy and Environmental Engineering, University of Science and Technology Beijing, Beijing, China

[4] Key Laboratory for Thermal Science and Power Engineering of Ministry of Education, Department of Engineering Mechanics, Tsinghua University, Beijing, China

Correspondence
Zhifeng Hu, Institute of Refrigeration and Cryogenics, MOE Engineering Research Center of Solar Power & Refrigeration, Shanghai Jiao Tong University, Shanghai 200240, China.
Email: hu_zhifeng@sjtu.edu.cn

Fuqiang Chu, School of Energy and Environmental Engineering, University of Science and Technology Beijing, Beijing 100083, China.
Email: chufq@ustb.edu.cn

Funding information
China Postdoctoral Science Foundation, Grant/Award Numbers: 2023TQ0210, GZB20230403; Beijing Natural Science Foundation, Grant/Award Number: 3242018; National Natural Science Foundation of China, Grant/Award Number: 52406104

Abstract

Droplet impact on solid surfaces is widely involved in diverse applications such as spray cooling, self-cleaning, and hydrovoltaic technology. Maximum solid–liquid contact area yielded by droplet spreading is one key parameter determining energy conversion between droplets and surfaces. However, for the maximum deformation of impact droplets, the contact length and droplet width are usually mixed indiscriminately, resulting in unignored prediction errors in the maximum contact area. Herein, we investigate and highlight the difference between the maximum contact length and maximum droplet width. The maximum droplet width is never smaller than the maximum contact length, and the difference appears once the contact angle exceeds 90° (which becomes more significant on superhydrophobic surfaces), regardless of impact velocities, liquid viscosities, and system scales (from macroscale to nanoscale). A theoretical model analyzing the structure of the spreading rim is proposed to demonstrate and quantitatively predict the above difference, agreeing well with experimental results. Based on molecular dynamics simulations, the theoretical analysis is further extended to the scenario of nanodroplets impacting on solid surfaces. Reconsideration on the maximum deformation of impact droplets underscores the often-overlooked yet significant difference between maximum values of contact length and droplet width, which is crucial for applications involving droplet–interface interactions.

INTRODUCTION

Nowadays, droplets play an increasingly important role in human life,[1–3] which keep participating in long-standing critical applications (such as spray cooling,[4] spray coating,[5] and crop irrigation[6]) and realize their potential in numerous emerging technologies (such as hydrovoltaics,[7] analyte detections,[8] and intelligent sensors[9]). The impact of liquid droplets on solid surfaces is a fundamental process in the above application areas, and relevant research has been receiving attention since the 19th century.[10] Droplets impacting on solid

---

Zhifeng Hu and Haojiang Ran contributed equally to this study.

surfaces usually experience drastic deformations in a short duration (typically within tens of milliseconds), causing various droplet behaviors such as jetting, splash, and breakup.[11,12] Depending on the properties of droplets and surfaces, droplet impact leads to different outcomes including deposition, partial rebound, and complete rebound.[13,14]

Despite the diversity of droplet impact, the droplet spreading length on solid surfaces is central to scientific studies, as it reflects the extent of direct solid–liquid interaction, which influences the exchange of momentum and energy between droplets and surfaces.[15–19] The maximum spreading length or maximum spreading coefficient (the ratio of the maximum spreading length to the droplet diameter) is considered as one of the key hydrodynamic parameters.[20,21] For instance, in heat transfer engineering, increasing the maximum spreading length is expected to improve the performance of thermal cooling,[22,23] while reducing the spreading length is conversely beneficial for anti-icing.[24,25] Besides, for droplet-based electricity generators, optimizing the electrical output requires elaborate adjustments of droplet impact positions to ensure that droplets contact the electrode at the maximum spreading.[26,27] Given the significance of the maximum spreading length, much effort has been devoted to developing theoretical prediction models. The classic model based on energy analysis is first proposed,[19,28] where the maximum spreading droplet is simplified as a cylindrical disk, and the maximum spreading length is given by the energy conversion between the initial spheric state and the cylindrical state. The energy-based model is continuously improved by modifying surface energy, kinetic energy, and viscous dissipations during droplet impact.[15,29] Scaling laws are established by connecting the maximum spreading length to dominated dimensionless numbers, and the Weber number and Reynolds number are mainly responsible for the low- and high-viscosity droplets, respectively.[17,18] Recently, the investigations of the maximum spreading length extend from millimeter-sized droplets to nanodroplets. At the nanoscale, the significant viscous effect and size effect lead to substantial changes in the maximum spreading length, and both the energy-based model and scaling laws should be reconfigured.[30,31] However, when applied to databases from different sources, current prediction models cannot provide satisfactory accuracy, and some may even produce large errors.[32,33]

Based on the detailed literature review, a simple yet significant issue is uncovered: the definition of the maximum spreading length is not unified and is divided into two types of characteristic lengths (Table S1).[15–19,28–30,33–44] As shown in Figure 1a, the droplet width W and contact length L of impact droplets both vary as the impact droplet deforms. The maximum droplet width W_{max} and the maximum contact length L_{max} are usually used indiscriminately to represent the maximum spreading length, with the usage of W_{max} and L_{max} accounts for nearly 50% and 50%, respectively (Figure 1b and Table S1). W_{max} reflects the maximum size of the droplet profile, affecting contacts between the droplet and other objects above the substrate. L_{max} represents the maximum contact between the droplet and the substrate, directly influencing solid–liquid energy and mass exchanges. For instance, the droplet width affects the droplet coalescence in water collection and condensation[45]; and the contact length matters for heat transfer in spray cooling[4] and contact electrification in droplet-based electricity generation.[27,46] On hydrophilic/superhydrophilic surfaces, the interchangeable usage of W_{max} and L_{max} is acceptable because the two quantities are equivalent (Figure 1c). However, on hydrophobic/superhydrophobic surfaces, W_{max} is usually greater than L_{max}, and thus the indiscrimination inevitably causes deviations (Figure 1d). Importantly, deviations in maximum spreading length bring unignored changes in the maximum spreading area because the area is proportional to the square of the length. Of note, a 10% deviation in length easily leads to a 20% error in area. Therefore, it is necessary to identify the maximum deformation of impact droplets on solid surfaces and clarify the difference between W_{max} and L_{max}.

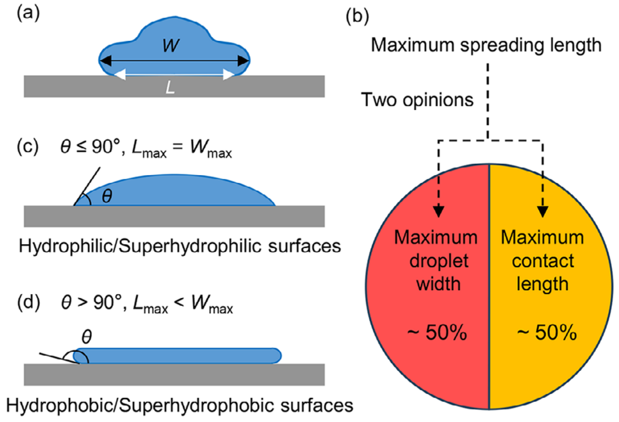

FIGURE 1 Schematics of the mixed spreading length. (a) Droplet width (W) and contact length (L) during droplet spreading. (b) Proportions of W_{max} and L_{max} taken as the maximum spreading length in literature, showing W_{max} and L_{max} are often mixed indiscriminately. Maximum deformation of impact droplets on (c) hydrophilic/superhydrophilic surfaces (where $L_{max} = W_{max}$) and (d) hydrophobic/superhydrophobic surfaces (where $L_{max} < W_{max}$). θ is the surface contact angle.

In this work, we begin with the experimental investigation on the temporal evolution of W and L, and identify the states for W_{max} and L_{max}. How the difference between W_{max} and L_{max} varies with important factors (including surface contact angle, droplet impact velocity, and liquid viscosity) is discussed, and the regions for unignored differences are highlighted. Furthermore, we establish a scaling law of the relative ratio between W_{max} and L_{max} based on the analysis of the rim structure near the contact line, which is shown to be valid for various conditions. Additionally, we extend the discussion and analysis from millimeter-sized droplets to nanodroplets, aiming to provide valuable instructions for droplet impact related applications in both macro- and nano-scale systems.

RESULTS AND DISCUSSION

Figure 2 shows the dynamic behaviors and deformation of droplets impacting on the superhydrophobic surface, which are captured by the high-speed photography. The hydrophobic surfaces and

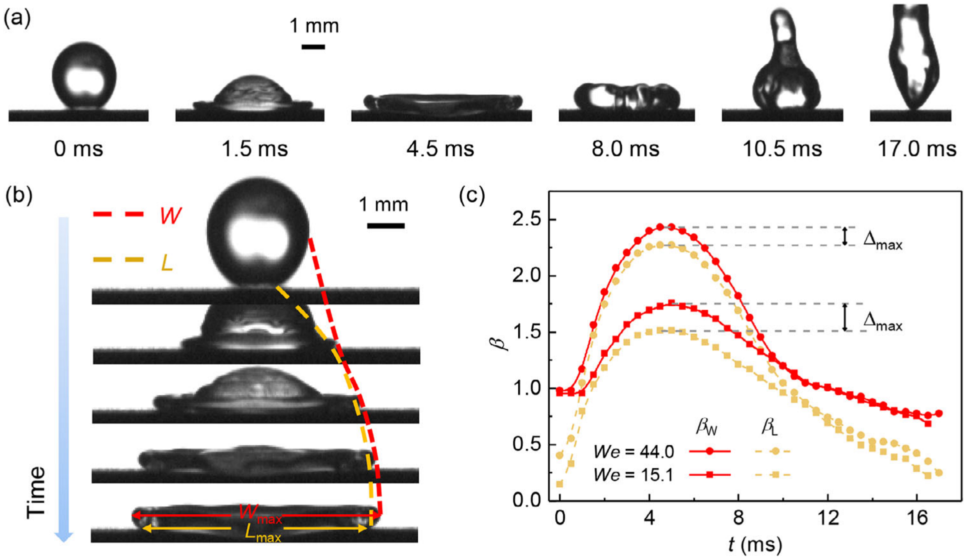

FIGURE 2 Dynamic behaviors and maximum deformation of droplets impacting on the superhydrophobic surface (with the advancing contact angle $\theta_a = 162°$). (a) Dynamic behaviors of impact droplets at $We = 44.0$. (b) Evolutions of the droplet width (W, red line) and contact length (L, orange line) during droplet spreading. (c) Time-varied droplet width coefficient β_W and contact length coefficient β_L at different We. Δ_{max} denotes the difference between $\beta_{W,max}$ and $\beta_{L,max}$.

superhydrophobic surfaces are fabricated through the spraying method. Detailed experimental methods are shown in Methods section. For low-viscosity liquid (e.g., deionized water), droplet deformations are controlled by the Weber number ($We = \rho D_0 U_0^2/\gamma$, where D_0 and U_0 are the diameter and impact velocity of droplets, ρ is the liquid density, and γ is the surface tension coefficient), which indicates the relative magnitude of inertial force and surface tension. In our experiments, for deionized water droplets, the diameter is $D_0 = 2.84$ mm, and U_0 is changed to adjust We.

Figure 2a displays the entire journey of the impact droplet on the superhydrophobic surface at $We = 44.0$. After the droplet contacts the surface, it spreads outwards till the maximum spreading state at 4.5 ms. Then, the spreading droplet gradually retracts inward, with the liquid converging to the center and moving upward, forming a vertically elongated shape. Eventually, the droplet completely rebounds from the superhydrophobic surface. Intuitively, the droplet width W keeps differing from the contact length L during the impact-rebound process. The temporal evolutions of W and L are compared and quantitatively described in Figure 2b,c. In the spreading stage, both W and L increase over time, reaching their maximum values simultaneously, with W always greater than L. The morphology of the maximum spreading droplet deviates from an oversimplified cylindrical disk. Particularly, the outermost gas–liquid interface deforms to a curved shape due to the effect of surface contact angle. The spreading of the contact line is constrained by the solid surface while the droplet width deforms more freely, leading to the noticeable difference between W_{max} and L_{max} (Figure 2b). In Figure 2c, W and L are nondimensionalized by the droplet diameter as $\beta_W = W/D_0$ and $\beta_L = L/D_0$, respectively. Correspondingly, the maximum width coefficient and maximum contact coefficient are $\beta_{W,max} = W_{max}/D_0$ and $\beta_{L,max} = L_{max}/D_0$, respectively. β_W–β_L cannot be overlooked for most of the duration, except the intermediate period of the spreading stage where the droplet rapidly flattens and expands because of the large inertial force. Δ_{max}, representing the difference between $\beta_{W,max}$ and $\beta_{L,max}$, is large and becomes greater at lower We. Δ_{max} is also affected by surface wettability, and reduces for a smaller surface contact angle (see Figure S2 for temporal evolutions of W and L on the hydrophobic surface).

Since the maximum deformations of impact droplets are largely affected by factors related to droplets and surfaces, $\beta_{W,max}$ and $\beta_{L,max}$ under different conditions are experimentally studied. As liquid viscosity alters the dominant factor influencing droplet deformations,[13,34] low- and high-viscosity fluids (the low and high viscosity is determined by the reported criterion[13,34]) are examined separately. Glycerin–water liquids of different glycerin volume fractions φ are prepared, and superamiphiphobic surfaces are fabricated (see Methods section for details).

First, for low-viscosity liquids, the droplet deformation is determined by the competition between inertial force and surface tension, and thus the variation of $\beta_{W,max}$ and $\beta_{L,max}$ with the Weber number is shown in Figure 3a. Both $\beta_{W,max}$ and $\beta_{L,max}$ increase with We due to the larger inertial force at higher We. As liquid viscosity rises, $\beta_{W,max}$ and $\beta_{L,max}$ decrease because droplet spreading is hindered by the enhanced viscous dissipation. The changes of $\beta_{W,max}$ and $\beta_{L,max}$ with We exhibit similar trends, and $\beta_{W,max}$–$\beta_{L,max}$ diminishes as We increases. Figure 3b shows the relative ratio $\beta_{W,max}/\beta_{L,max}$ at different We. To maintain 90% accuracy in the spreading area, the deviation in the maximum spreading length should be below 5%, that is, $\beta_{W,max}/\beta_{L,max} \leq 1.05$. On superhydrophobic surfaces, $\beta_{W,max}/\beta_{L,max}$ exceeds 1.1 at $We < 40$ with the corresponding change in contact area greater than 21%. As We reaches around 80, $\beta_{W,max}/\beta_{L,max}$ approaches 1.05 with about 10% deviation in contact area. Therefore, for superhydrophobic surfaces, distinguishing between droplet width and contact length is crucial to avoid significant

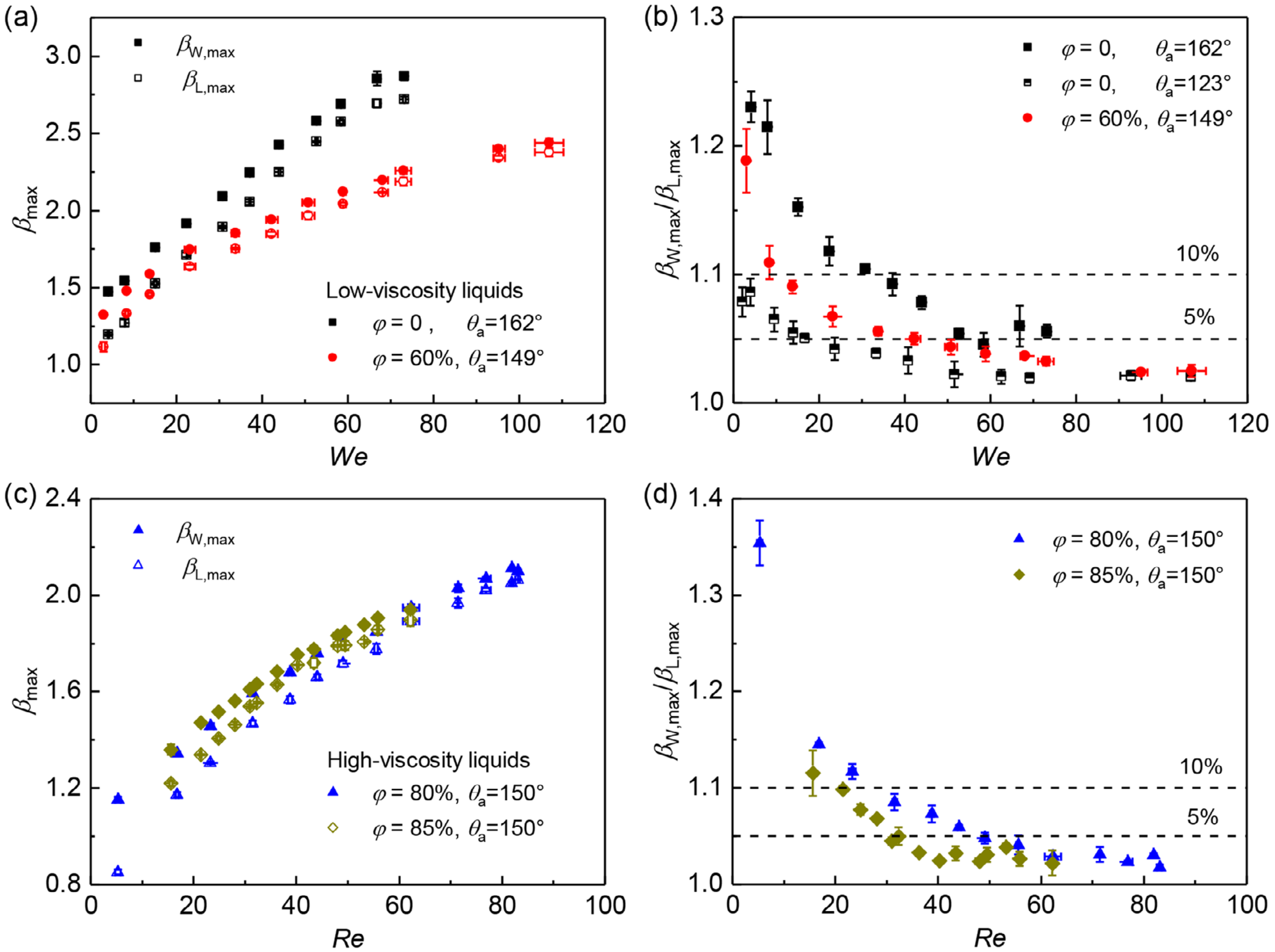

FIGURE 3 Variations of maximum width coefficient $\beta_{\mathrm{W,max}}$ and maximum contact coefficient $\beta_{\mathrm{L,max}}$. For low-viscosity liquids, (a) $\beta_{\mathrm{W,max}}$ and $\beta_{\mathrm{L,max}}$ as a function of *We*, and (b) $\beta_{\mathrm{W,max}}/\beta_{\mathrm{L,max}}$ as a function of *We*. For high-viscosity liquids, (c) $\beta_{\mathrm{W,max}}$ and $\beta_{\mathrm{L,max}}$ as a function of *Re*, and (d) $\beta_{\mathrm{W,max}}/\beta_{\mathrm{L,max}}$ as a function of *Re*. Dashed lines in (b) and (d) denote relative differences of 5% and 10%.

calculation or prediction errors. When shifting superhydrophobic surfaces to hydrophobic surfaces, remarkable reductions in $\beta_{\mathrm{W,max}}/\beta_{\mathrm{L,max}}$ are observed. $\beta_{\mathrm{W,max}}/\beta_{\mathrm{L,max}}$ hardly reaches 1.1 even at very low *We*, and $\beta_{\mathrm{W,max}}/\beta_{\mathrm{L,max}}$ quickly decreases below 1.05 at $We > 20$. Besides, the increase of liquid viscosity also leads to the reduction of $\beta_{\mathrm{W,max}}/\beta_{\mathrm{L,max}}$, where $\beta_{\mathrm{W,max}}/\beta_{\mathrm{L,max}}$ for liquids of $\varphi = 60\%$ becomes smaller than 1.05 at $We > 40$.

For high-viscosity liquids, the droplet deformation is driven by the interplay of inertial force and viscous stress, so the variation of $\beta_{\mathrm{W,max}}$ and $\beta_{\mathrm{L,max}}$ with the Reynolds number ($Re = \rho D_0 U_0/\mu$, where μ is the dynamic viscosity) on superamiphiphobic surfaces is shown in Figure 3c. Due to the significant role of viscous effect, droplet spreading is suppressed, and values of $\beta_{\mathrm{W,max}}$, $\beta_{\mathrm{L,max}}$ and $\beta_{\mathrm{W,max}}–\beta_{\mathrm{L,max}}$ for high-viscosity liquids are generally smaller than those for low-viscosity liquids. As displayed in Figure 3d, $\beta_{\mathrm{W,max}}/\beta_{\mathrm{L,max}}$ decreases with increasing *Re* and is smaller for liquids with higher viscosity. The *Re* thresholds for $\beta_{\mathrm{W,max}}/\beta_{\mathrm{L,max}} = 1.05$ are approximately 50 and 30 for liquids of $\varphi = 80\%$ and 85%, respectively. Figure 3b,d shows the need to recognize the difference between $\beta_{\mathrm{W,max}}$ and $\beta_{\mathrm{L,max}}$, particularly for droplets with low liquid viscosity impacting on surfaces of high contact angles at small impact velocities, where discrepancies in maximum spreading area easily exceed 20% or even more.

To further reveal the mechanism underlying the disparity between the maximum droplet width and maximum contact length, the cross-section schematic of the maximum deformed droplet is shown in Figure 4a. Here, $W_{\max}$ and $L_{\max}$ are assumed to occur simultaneously because the time difference for reaching $W_{\max}$ and $L_{\max}$ is typically around 0.2 ms (Figure S3) and both *W* and *L* change slowly around the maximum deformation time (Figures 2c and S2b). At the maximum spreading, a lamella-rim structure tends to be formed,[20,54] with the thin liquid film in the middle connecting thick rims. The cross-sectional profile of the outer rim is simplified as a truncated circle of a radius R_{rim} (enlarged view in Figure 4a). Given a contact angle larger than 90°, the difference between $W_{\max}$ and $L_{\max}$ appears, and its value is expressed as,

$$\frac{W_{\max}}{2} - \frac{L_{\max}}{2} = R_{\mathrm{rim}}\left[1 - \cos\left(\theta_a - \frac{\pi}{2}\right)\right] \tag{1}$$

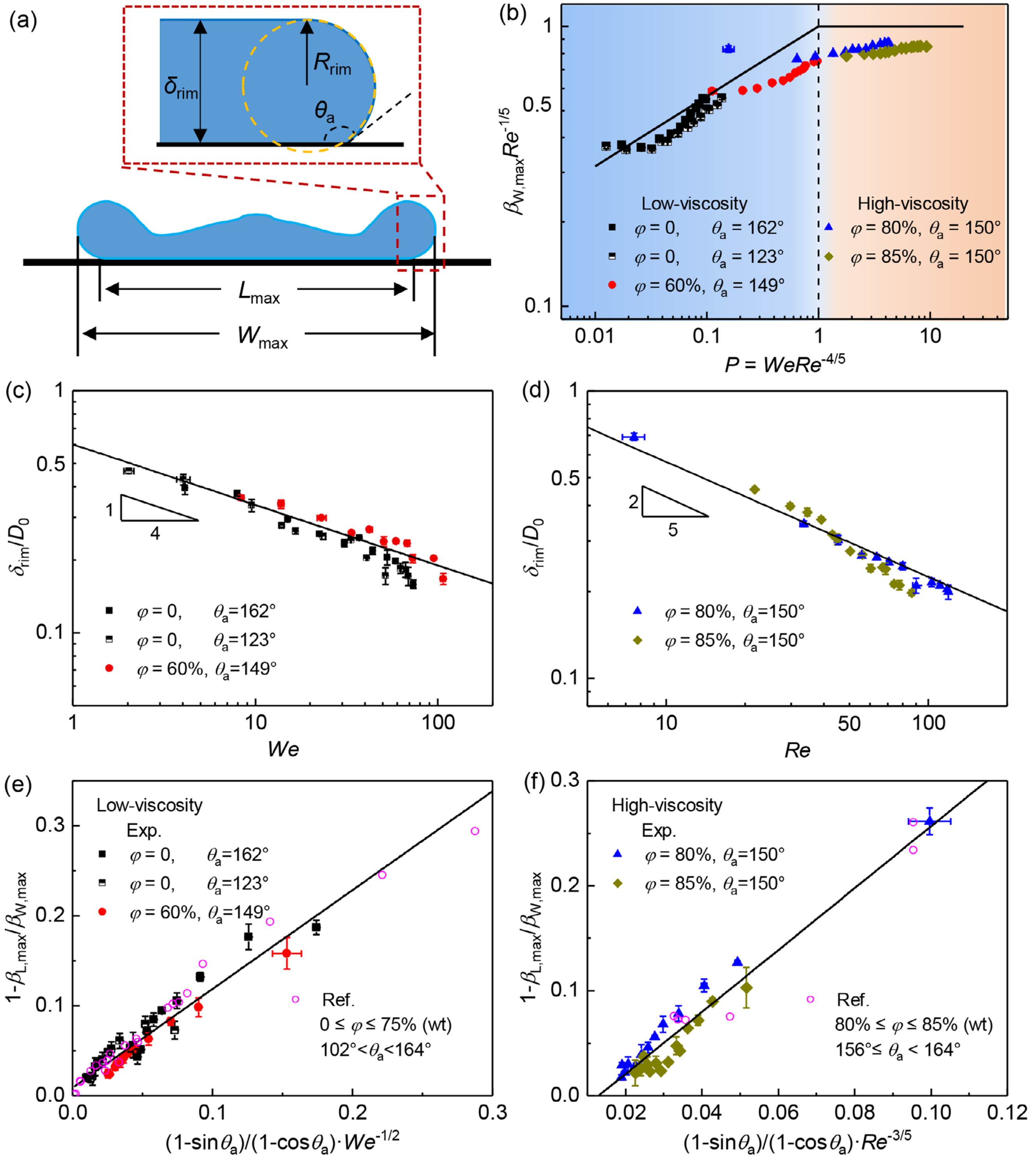

FIGURE 4 Relationship between the maximum width coefficient $\beta_{W,max}$ and the maximum contact length coefficient $\beta_{L,max}$. (a) The cross-section schematic of the maximum deformed droplet. The enlarged view shows the geometric relationships of the rim. (b) Universal law of $\beta_{W,max}$ for droplets with different viscosities. Variation of $\beta_{W,max}$ with the impact parameter P. Solid lines present the scaling laws. Dimensionless thickness of rims at the maximum deformation as a function of (c) We for low-viscosity liquids and (d) Re for high-viscosity liquids. Theoretical predictions of $1-\beta_{L,max}/\beta_{W,max}$ for (e) low-viscosity liquids and (f) high-viscosity liquids. Reference data are extracted from literature reported by 10 different research groups.[34,35,43,47–53] "wt" denotes the mass fraction of glycerin–water mixtures.

R_{rim} is related to the thickness of the rim δ_{rim}, and the geometric relationship gives,

$$\delta_{\mathrm{rim}} = R_{\mathrm{rim}}\left[1 + \sin\left(\theta_a - \frac{\pi}{2}\right)\right] \tag{2}$$

Then, Equation (1) can be written in a dimensionless form,

$$\frac{1}{2}\left(\beta_{\mathrm{W,max}} - \beta_{\mathrm{L,max}}\right) = \frac{1-\sin\theta_a}{1-\cos\theta_a}\frac{\delta_{\mathrm{rim}}}{D_0} \tag{3}$$

Considering the robustness of existing models, the scaling law proposed by Clanet et al.[18] is adopted to describe the maximum width coefficient $\beta_{\mathrm{W,max}}$,

$$\beta_{\mathrm{W,max}} \sim \begin{cases} We^{1/4}, & P \le 1 \\ Re^{1/5}, & P < 1 \end{cases} \tag{4}$$

where the impact parameter for millimeter-sized droplets is $P = WeRe^{-4/5}$. Figure 4b shows that Equation (4) matches our experimental data for both $P \le 1$ (for low-viscosity liquids) and $P > 1$ (for high-viscosity liquids).

The dimensionless rim thickness $\delta_{\mathrm{rim}}/D_0$ under different conditions are presented in Figure 4c,d, and the fitting of experimental data gives,

$$\frac{\delta_{\mathrm{rim}}}{D_0} \sim \begin{cases} We^{-1/4}, & P \le 1 \\ Re^{-2/5}, & P > 1 \end{cases} \tag{5}$$

Note that Equation (5) is close to the correlation of the average film thickness calculated from the volume conservation of a simplified cylindrical disk (i.e., $\delta_{\mathrm{rim}}/D_0 \sim 1/\beta^2_{\mathrm{W,max}}$). However, the actual shape of the lamella-rim structure features a thinner center and thicker rim, which is evident at lower viscosity.[36,55] This leads to the deviation in the fitting equation at $P \le 1$ while maintaining the same form at $P > 1$. Combining Equations (3)–(5), we eventually obtain the scaling law of $\beta_{\mathrm{W,max}}/\beta_{\mathrm{L,max}}$,

$$1 - \frac{\beta_{\mathrm{L,max}}}{\beta_{\mathrm{W,max}}} \sim \begin{cases} \frac{1-\sin\theta_a}{1-\cos\theta_a} We^{-1/2}, & P \le 1 \\ \frac{1-\sin\theta_a}{1-\cos\theta_a} Re^{-3/5}, & P > 1 \end{cases} \tag{6}$$

Alongside our experimental results, literature data from different research groups[34,35,43,47–53] are included to verify the accuracy of our theoretical model. As shown in Figure 4e,f, regardless of droplet parameters and surface wettability, all data collapse onto the principal curves determined by Equation (6), demonstrating the validity and reliability of the established model. Equation (6) provides an intuitive explanation for the decrease of $\beta_{\mathrm{W,max}}/\beta_{\mathrm{L,max}}$ at higher We or Re. Also, since $(1 - \sin\theta_a)/(1 - \cos\theta_a)$ increases monotonically within the range of $90^\circ \le \theta_a < 180^\circ$ (Figure S4), $\beta_{\mathrm{W,max}}/\beta_{\mathrm{L,max}}$ rises when the surface becomes more hydrophobic. Additionally, slight deviations of data from the prediction curves at lower We or Re are mainly attributed to the less deformed droplet morphology constrained by surface tension or viscous stress.

Apart from commonly studied millimeter-sized droplets, nanodroplets have also garnered considerable attention due to their important roles in nanotechnology. To explore how the dimension of droplets affects the difference between W_{max} and L_{max}, the system of droplet impact is extended from the macroscale to the nanoscale. The maximum deformation of nanodroplets impacting on superhydrophobic surfaces is further examined through molecular dynamics (MD) simulations (see Method section for details). Figure 5a shows the dynamic behaviors of water nanodroplets impacting on the superhydrophobic surface. The impact nanodroplet experiences spreading, retraction and rebound in sequence, which is similar to the process of millimeter-sized droplets (Figure 2a). Importantly, despite the reduction of length from millimeters to nanometers, the difference between W and L consistently appears during the spreading and retraction, and W_{max}–L_{max} remains apparent at the maximum deformation (Figure 5b,c).

As the Weber number increases, $\beta_{\mathrm{W,max}}/\beta_{\mathrm{L,max}}$ generally decreases. $\beta_{\mathrm{W,max}}/\beta_{\mathrm{L,max}}$ is larger than 1.1 at $We < 40$, and falls below 1.05 at $We > 100$ (Figure 6a). Since the formation of the rim is observed, Equation (3) derived from the analysis of the rim structure remains applicable to nanodroplets. Thanks to the recent research on the spreading of nanodroplets, $\beta_{\mathrm{L,max}}$ can be expressed as,[30]

$$\beta_{\mathrm{L,max}} \sim \begin{cases} We^{1/5}, & Q \le 2.1 \\ We^{1/2}Oh^{1/3}, & Q > 2.1 \end{cases} \tag{7}$$

where the impact parameter for nanodroplets is $Q = We^{3/10}Oh^{1/3}$, and the Ohnesorge number $[Oh = \mu/(\rho D_0 \gamma)^{1/2}]$ reflects the viscous effect and size effect on droplet dynamics. Oh at the nanoscale is nearly two orders of magnitudes larger than that at the macroscale (with $Oh = 0.35$ for $D_0 = 10$ nm while $Oh = 0.00226$ for $D_0 = 2$ mm), indicating the significantly enhanced viscous impedance. Therefore, even for low-viscosity liquids, scaling laws are divided into two regimes (as shown in Equation 7). Figure 6b shows that $\beta_{\mathrm{L,max}}$ of nanodroplets well follows Equation (7). In the capillary regime ($Q \le 2.1$), $\beta_{\mathrm{L,max}}$ is a function of We because the capillary force and inertial force dominate the droplet deformation, while in the cross-over regime ($Q > 2.1$), the viscous force becomes another important factor, and $\beta_{\mathrm{L,max}}$ is related to both We and Oh.

The dimensionless rim thickness of maximum spreading nanodroplets in Equation (3) is observed to satisfy the following equation (Figure 6c),

$$\frac{\delta_{\mathrm{rim}}}{D_0} \sim We^{-2/5} \tag{8}$$

Equation (8) approaches the average film thickness at $Q \le 2.1$, that is $\delta_{\mathrm{rim}}/D_0 \sim 1/\beta^2_{\mathrm{L,max}} \sim We^{-2/5}$, which is attributed to the uniform distribution of liquid film thickness at low We (Figure 2a). However, at $Q > 2.1$, the difference in thickness between the rim and inner film is formed due to high We,[56] which leaves $\delta_{\mathrm{rim}}/D_0$ deviating from $1/\beta^2_{\mathrm{L,max}}$ but showing a trend consistent with that observed at $Q \le 2.1$. By integrating Equations (7) and (8) into Equation (3), we obtain

$$\frac{\beta_{\mathrm{W,max}}}{\beta_{\mathrm{L,max}}} - 1 \sim \begin{cases} \frac{1-\sin\theta_a}{1-\cos\theta_a} We^{-3/5}, & Q \le 2.1 \\ \frac{1-\sin\theta_a}{1-\cos\theta_a} We^{-9/10}Oh^{-1/3}, & Q > 2.1 \end{cases} \tag{9}$$

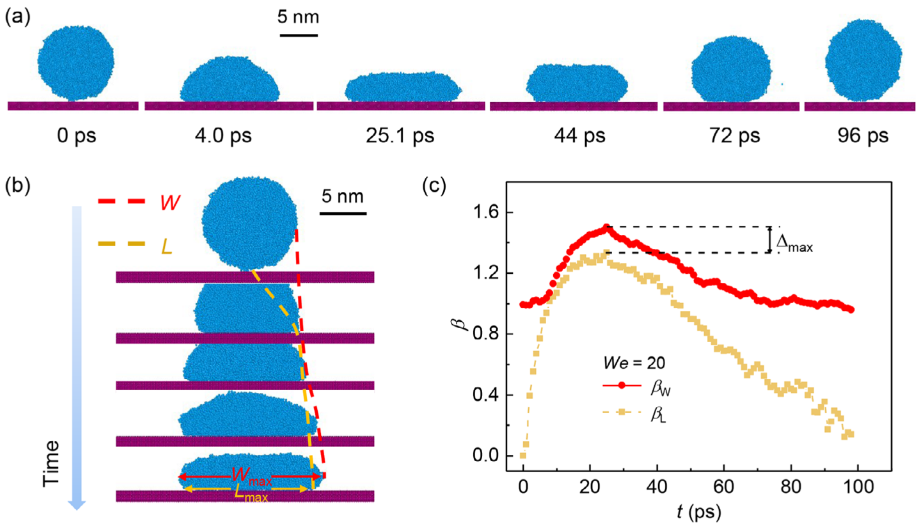

FIGURE 5 Dynamic behaviors and maximum deformation of nanodroplets impacting on the superhydrophobic surface (with the static contact angle $\theta_s = 160°$). (a) Dynamic behaviors of impact nanodroplets at $We = 20$. (b) Evolution of the droplet width (W, red line) and contact length (L, orange line) during droplet spreading. (c) Time-varied droplet width coefficient β_W and contact length coefficient β_L at $We = 20$. Δ_{max} denotes the difference between $\beta_{W,max}$ and $\beta_{L,max}$.

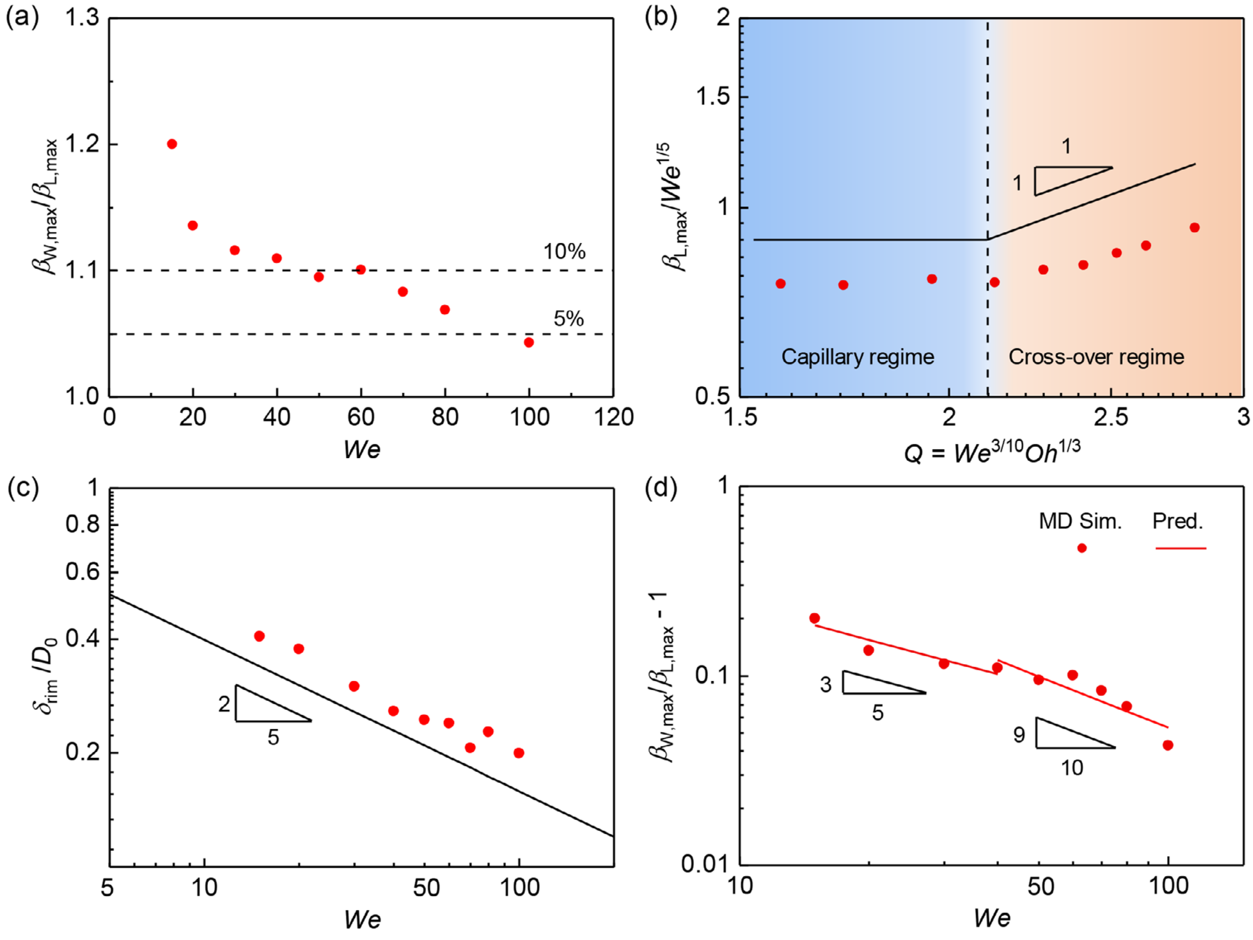

FIGURE 6 Relationship between maximum width coefficient $\beta_{W,max}$ and maximum contact length coefficient $\beta_{L,max}$ for nanodroplets. (a) $\beta_{W,max}/\beta_{L,max}$ as a function of We. Dashed lines denote the difference of 5% and 10%. (b) Universal law of $\beta_{L,max}$. Variation of $\beta_{L,max}$ with the impact parameter Q for nanodroplets at different regimes. (c) Dimensionless thickness of rims at the maximum deformation as a function of We. Solid lines in (b) and (c) present the governing laws. (d) Theoretical prediction of $\beta_{W,max}/\beta_{L,max} - 1$ for nanodroplets. Solid lines show the theoretical line determined by the predictive model.

Equation (9) indicates that $\beta_{W,max}/\beta_{L,max}$ initially decreases slowly and then quickly with increasing We, a trend clearly illustrated in Figure 6d. The power exponents of We, –3/5 and –9/10, are close to the fitting values –0.58 and –0.95 at $Q \leq 2.1$ and >2.1, respectively. The predicted values are consistent with MD simulation data. Therefore, at the nanoscale, the difference between W_{max} and L_{max} remains primarily governed by the rim structure originated from the surface contact angle.

CONCLUSIONS

In conclusion, the maximum deformation of impact droplets on solid surfaces leads to the maximum spreading length, which is well-known for the significant contribution in exchanges of mass and energy between solid and liquid phases. We emphasize the lack of consensus on the definition of maximum spreading length, which is often viewed as two different characteristic lengths (i.e., the maximum droplet width or maximum contact length), leading to errors in calculations. Our work reveals that the maximum droplet width is inevitably larger than the maximum contact length when the contact angle is over 90°, due to the protruding rim near the contact line caused by the inherent contact angle. The variations in the difference between the two characteristic lengths are investigated across various factors. The difference is unignored and becomes more noticeable at lower impact velocities, liquid viscosities, and larger surface contact angles, potentially exceeding 10%, which yields a 20% error in contact area. Particular attention should be paid to droplets impacting on superhydrophobic surfaces, the threshold Weber number for the 10% deviation in contact area is as high as about 80. We quantify the difference by analyzing the geometry relationships of the rim structure, and further establish the reliable scaling laws for the ratio of the maximum droplet width to the maximum contact length. For both macroscale and nanoscale systems, predictions from scaling laws agree well with the experimental, simulation and literature data, hoping to offer useful guidance on the utilization of droplet impact. Learning from the findings, we would highlight that the maximum droplet width and maximum contact length are interconnected, but their distinction should be carefully recognized in different application sceneries. In future work, to fully understand droplet impact dynamics across scales from nm to mm, the maximum deformation of micrometer-sized droplets should be studied, potentially using lattice Boltzmann methods.[57,58] Furthermore, it is crucial to clarify the effect of surface structures on the maximum deformation of droplets, which can significantly alter droplet spreading dynamics.[21,50]

METHODS

Droplet impact experiments: three kinds of solid surfaces with different wettabilities are fabricated. Polytetrafluoroethylene plate is used as the hydrophobic surface. Commercial coating solutions of superhydrophobicity (Schanda Co., Ltd.) and superamphiphobicity (Sysmyk CCP0002 and CCP0003) are sprayed on bare aluminum surfaces to fabricate the superhydrophobic surface and superamphiphobic surface, respectively.[59] The surface micromorphology is characterized by the scanning electronic microscope (SEM, Zeiss Merlin), and SEM images are shown in Figure S1. Surface contact angles are measured by the contact-angle goniometer (JC2000C1). Static, advancing, and receding contact angles (θ_s, θ_a, θ_r) are listed in Table S2.

Glycerin–water mixture liquid with different glycerin volume fractions φ is prepared by directly mixing deionized water (AR, Titan Technology Co., Ltd.) and glycerin (≥99.0%, Titan Technology Co., Ltd.). The liquid properties and droplet diameters of glycerin–water mixtures are listed in Table S3. Glycerin–water mixture solutions are added into the syringe pump (LSP02-1Y) to generate droplets. The releasing heights and impact positions of droplets are both adjustable through the three-axis platform. A high-speed camera (Revealer X113M) along with the illumination device (Hecho S5000) are applied to capture the dynamic process of droplet impact. Experimental images are processed using Matlab.

MD simulations: MD simulations are carried out on the large-scale atomic/molecular massively parallel simulator. We simulate the water nanodroplets impacting on superhydrophobic platinum substrate. The computational box is in the dimension of $40 \times 40 \times 30$ nm^3, where the diameter of nanodroplets is set as 10 nm (Figure S5a). The bottom boundary is a superhydrophobic wall with a static contact angle of $\theta_s = 160°$ (Figure S5b), and the top plane is set as a reflecting wall. The surrounding planes are set as periodic boundaries. The Lennard–Jones potential is used to describe the interactions of platinum–platinum and water–platinum.[30] The monatomic water model is applied to model water molecules.[60] The parameters used in the simulations are summarized in Table S4. We use the Nosé–Hoover thermostat method to reach the equilibrium of the system, and then the nanodroplet is released with a given velocity to impact the surface (detailed procedures are shown in Ref. 30). The simulations last until the nanodroplets rebound from the surface.

ACKNOWLEDGMENTS

We acknowledge financial support from the China Postdoctoral Science Foundation (nos. 2023TQ0210, GZB20230403), the Beijing Natural Science Foundation (no. 3242018), and the National Natural Science Foundation of China (no. 52406104).

CONFLICT OF INTEREST STATEMENT

The authors declare no conflicts of interest.

ORCID

Zhifeng Hu https://orcid.org/0000-0003-2921-8575
Fuqiang Chu https://orcid.org/0000-0002-4054-143X

REFERENCES

1. Hu Z, Chu F, Shan H, Wu X, Dong Z, Wang R. Understanding and utilizing droplet impact on superhydrophobic surfaces: phenomena, mechanisms, regulations, applications, and beyond. *Adv Mater.* 2024;36:202310177.

2. Wang X, Xu B, Guo S, Zhao Y, Chen Z. Droplet impacting dynamics: recent progress and future aspects. *Adv Colloid Interface Sci*. 2023;317:102919.
3. Zhao Z, Li H, Liu Q, et al. Regulating droplet impact symmetry by surface engineering. *Droplet*. 2023;2:e52.
4. Jiang M, Wang Y, Liu F, et al. Inhibiting the Leidenfrost effect above 1,000 °C for sustained thermal cooling. *Nature*. 2022;601:568-572.
5. Park N, Zhu K. Scalable fabrication and coating methods for perovskite solar cells and solar modules. *Nat Rev Mater*. 2020;5:333-350.
6. Liu S, Zhang C, Shen T, et al. Efficient agricultural drip irrigation inspired by fig leaf morphology. *Nat Commun*. 2023;14:5934.
7. Wang X, Lin F, Wang X, et al. Hydrovoltaic technology: from mechanism to applications. *Chem Soc Rev*. 2022;51:4902-4927.
8. Li H, Fang W, Zhao Z, et al. Droplet precise self-splitting on patterned adhesive surfaces for simultaneous multidetection. *Angew Chem Int Ed*. 2020;59:10535-10539.
9. Xu X, Li P, Ding Y, et al. Droplet energy harvesting panel. *Energy Environ Sci*. 2022;15:2916.
10. Worthington AM. On the forms assumed by drops of liquids falling vertically on a horizontal plate. *Proc R Soc Lond*. 1876;25:261.
11. Yarin AL. Drop impact dynamics: splashing, spreading, receding, bouncing. *Annu Rev Fluid Mech*. 2006;38:159-192.
12. Chu F, Li S, Hu Z, Wu X. Regulation of droplet impacting on superhydrophobic surfaces: coupled effects of macrostructures, wettability patterns, and surface motion. *Appl Phys Lett*. 2023;122:160503.
13. Lin S, Zhao B, Zou S, Guo J, Wei Z, Chen L. Impact of viscous droplets on different wettable surfaces: impact phenomena, the maximum spreading factor, spreading time and post-impact oscillation. *J Colloid Interface Sci*. 2018;516:86-97.
14. Li Y, Wu X, Lin Y, Hu Z. Dynamics and maximum spreading of droplet impact on a stationary droplet on the surface. *Int J Mech Sci*. 2024;274:109272.
15. Wang F, Yang L, Wang L, Zhu Y, Fang T. Maximum spread of droplet impacting onto solid surfaces with different wettabilities: adopting a rim-lamella shape. *Langmuir*. 2019;35:3204-3214.
16. Wildeman S, Visser CW, Sun C, Lohse D. On the spreading of impacting drops. *J Fluid Mech*. 2016;805:636-655.
17. Laan N, de Bruin KG, Bartolo D, Josserand C, Bonn D. Maximum diameter of impacting liquid droplets. *Phys Rev Appl*. 2014;2:44018.
18. Clanet C, Beguin C, Denis R, Quéré D. Maximal deformation of an impacting drop. *J Fluid Mech*. 2004;517:199-208.
19. Pasandideh-Fard M, Qiao YM, Chandra S, Mostaghimi J. Capillary effects during droplet impact on a solid surface. *Phys Fluids*. 1996;8:650.
20. Hu Z, Chu F, Wu X. Double-peak characteristic of droplet impact force on superhydrophobic surfaces. *Extreme Mech Lett*. 2022;52:101665.
21. Hu Z, Zhang X, Gao S, et al. Axial spreading of droplet impact on ridged superhydrophobic surfaces. *J Colloid Interface Sci*. 2021;599:130-139.
22. Guo C, Maynes D, Crockett J, Zhao D. Heat transfer to bouncing droplets on superhydrophobic surfaces. *Int J Heat Mass Transf*. 2019;137:857-867.
23. Zhu Z, Chen Y, Luo X, et al. Ultrafast impact superspreading on superamphiphilic silicon surfaces for effective thermal management. *J Am Chem Soc*. 2023;145:15128-15136.
24. Chu F, Hu Z, Feng Y, Lai N-C, Wu X, Wang R. Advanced anti-icing strategies and technologies by macrostructured photothermal storage superhydrophobic surfaces. *Adv Mater*. 2024;36:2402897.
25. Kumar V, Fu Q, Szeto H, Zhu Y. Heat transfer during droplet impact on a cold superhydrophobic surface via interfacial thermal mapping. *Droplet*. 2024;3:e124.
26. Li L, Li X, Deng W, et al. Sparking potential over 1200 V by a falling water droplet. *Sci Adv*. 2023;9:eadi2993.
27. Xu W, Zheng H, Liu Y, et al. A droplet-based electricity generator with high instantaneous power density. *Nature*. 2020;578:392-396.
28. Chandra S, Avedisian CT. On the collision of a droplet with a solid surface. *Pro R Soc A*. 1991;432:13-41.
29. Ukiwe C, Kwok DY. On the maximum spreading diameter of impacting droplets on well-prepared solid surfaces. *Langmuir*. 2005;21:666-673.
30. Wang Y, Wang Y, He X, et al. Scaling laws of the maximum spreading factor for impact of nanodroplets on solid surfaces. *J Fluid Mech*. 2022;937:A12.
31. Wang Y, Wang Y, Gao S, Yang Y, Wang X, Chen M. Universal model for the maximum spreading factor of impacting nanodroplets: from hydrophilic to hydrophobic surfaces. *Langmuir*. 2020;36:9306-9316.
32. Aksoy YT, Eneren P, Koos E, Vetrano MR. Spreading of a droplet impacting on a smooth flat surface: how liquid viscosity influences the maximum spreading time and spreading ratio. *Phys Fluids*. 2022;34:042106.
33. Liang G, Chen Y, Chen L, Shen S. Maximum spreading for liquid drop impacting on solid surface. *Ind Eng Chem Res*. 2019;58:10053-10063.
34. Tai Y, Xu H, Bai Y, Li L, Wang S, Xia Z. Experimental investigation of the impact of viscous droplets on superamphiphobic surfaces. *Phys Fluids*. 2022;34:022101.
35. Wang R, Shi Y, Zhang C, Ding H. On the maximal spreading of drops impacting onto a no-slip substrate. *Phys Fluids*. 2022;34:052103.
36. Guo J, Lin S, Zhao B, Deng X, Chen L. Spreading of impinging droplets on nanostructured superhydrophobic surfaces. *Appl Phys Lett*. 2018;113:71602.
37. Liu H, Zhang C, Gao P, Lu X, Ding H. On the maximal spreading of impacting compound drops. *J Fluid Mech*. 2018;854:R6.
38. Lee JB, Laan N, de Bruin KG, et al. Universal rescaling of drop impact on smooth and rough surfaces. *J Fluid Mech*. 2016;786:R4.
39. Visser CW, Tagawa Y, Sun C, Lohse D. Microdroplet impact at very high velocity. *Soft Matter*. 2015;8:10732-10737
40. Tran T, Staat HJJ, Susarrey-Arce A, et al. Droplet impact on superheated micro-structured surfaces. *Soft Matter*. 2013;9:3272.
41. Zhou Y, Zhang C, Zhao W, Wang S, Zhu P. Suppression of hollow droplet rebound on super-repellent surfaces. *Nat Commun*. 2023;14:5386.
42. Fernández-Toledano JC, Braeckeveldt B, Marengo M, De Coninck J. How wettability controls nanoprinting. *Phys Rev Lett*. 2020;124:224503.
43. Yonemoto Y, Kunugi T. Analytical consideration of liquid droplet impingement on solid surfaces. *Sci Rep*. 2017;7:2362.
44. Moitra S, Elsharkawy M, Russo A, et al. Droplet orthogonal impact on nonuniform wettability surfaces. *Droplet*. 2023;2:e63.
45. Li M, Yu H, Liu Z, Gao Z, Chen F. Quantitative liquid storage by billiards-like droplet collision on surfaces with patterned wettability. *Droplet*. 2024;3:e125.
46. Hu Z, Zhong H, Shan H, Wang R. Quick evaluation and regulation of the maximum instantaneous power and matching resistance for droplet-based electricity generators. *Nano Res*. 2024;17:9999-10007.
47. Lee JB, Derome D, Dolatabadi A, Carmeliet J. Energy budget of liquid drop impact at maximum spreading: numerical simulations and experiments. *Langmuir*. 2016;32:1279-1288.
48. Gao S, Wei B, Jin J, et al. Contact time of a droplet impacting hydrophobic surfaces. *Phys Fluids*. 2022;34:067104.
49. Zhang X, Zhu Z, Zhang C, Yang C. Reduced contact time of a droplet impacting on a moving superhydrophobic surface. *Appl Phys Lett*. 2020;17:151602.
50. Bird JC, Dhiman R, Kwon H, Varanasi KK. Reducing the contact time of a bouncing drop. *Nature*. 2013;503:385-388.
51. Abolghasemibizaki M, Dilmaghani N, Mohammadi R, Castano CE. Viscous droplet impact on nonwettable textured surfaces. *Langmuir*. 2019;35:10752-10761.
52. Zhao B, Wang X, Zhang K, Chen L, Deng X. Impact of viscous droplets on superamphiphobic surfaces. *Langmuir*. 2017;33:144.

53. Deng X, Schellenberger F, Papadopoulos P, Vollmer D, Butt H. Liquid drops impacting superamphiphobic coatings. *Langmuir*. 2013;29:7847-7856.
54. Wang F, Fang T. Retraction dynamics of water droplets after impacting upon solid surfaces from hydrophilic to superhydrophobic. *Phys Rev Fluids*. 2020;5:033604.
55. Lin S, Wang Y, Sun L, Mehrizi AA, Jin Y, Chen L. Experimental and numerical investigations on the spreading dynamics of impinging liquid droplets on diverse wettable surfaces. *Int J Multiph Flow*. 2022;153:104135.
56. Wang Y, Wang Y, Zhang C, et al. Retraction and bouncing dynamics of nanodroplets upon impact on superhydrophobic surfaces. *Phys Fluids*. 2023;35:032012.
57. Wang G, Fei L, Luo KH. Unified lattice Boltzmann method with improved schemes for multiphase flow simulation: application to droplet dynamics under realistic conditions. *Phys Rev E*. 2022;105:045314.
58. Fei L, Qin F, Wang G, et al. Coupled lattice Boltzmann method—discrete element method model for gas–liquid–solid interaction problems. *J Fluid Mech*. 2023;975:A20.
59. Hu Z, Chu F, Wu X, Ding S, Lin Y. Bidirectional transport of split droplets. *Phys Rev Appl*. 2022;18:044057.
60. Molinero V, Moore EB. Water modeled as an intermediate element between carbon and silicon. *J Phys Chem B*. 2009;113:4008-4016.

SUPPORTING INFORMATION

Additional supporting information can be found online in the Supporting Information section at the end of this article.

How to cite this article: Hu Z, Ran H, Shan H, Chu F, Wang Z, Wang R. Reconsideration on the maximum deformation of droplets impacting on solid surfaces. *Droplet*. 2025;4:e163. https://doi.org/10.1002/dro2.163